

Constraining the reionization history with CMB and spectroscopic observations

Wei-Ming Dai^{1,3,4,*}, Yin-Zhe Ma^{3,4,†}, Zong-Kuan Guo^{1,2,‡} and Rong-Gen Cai^{1,2,§}

¹*CAS Key Laboratory of Theoretical Physics, Institute of Theoretical Physics,
Chinese Academy of Sciences, P.O. Box 2735, Beijing 100190, China*

²*School of Physical Sciences, University of Chinese Academy of Sciences, No. 19A Yuquan Road, Beijing 100049, China*

³*School of Chemistry and Physics, University of KwaZulu-Natal,
Westville Campus, Private Bag X54001, Durban, 4000, South Africa*

⁴*NAOC-UKZN Computational Astrophysics Centre (NUCAC),
University of KwaZulu-Natal, Durban, 4000, South Africa*

We investigate the constraints on the reionization history of the Universe from a joint analysis of the cosmic microwave background and neutral hydrogen fraction data. The tanh parametrization and principal component analysis methods are applied to the reionization history respectively. The commonly used tanh parametrization is oversimplistic when the neutral hydrogen fraction data are taken into account. Using the principal component analysis method, the reconstructed reionization history is consistent with the neutral hydrogen fraction data. With the principal component analysis method, we reconstruct the neutral hydrogen fraction at $z = 9.75$ as $x_{\text{HI}} = 0.69_{-0.32}^{+0.30}$ for $6 < z < 20$ range reconstruction, and $x_{\text{HI}} = 0.76_{-0.27}^{+0.22}$ for $6 < z < 30$ range reconstruction. These results suggest that the Universe began to reionize at redshift no later than $z = 10$ at a 95% confidence level.

1. INTRODUCTION

The observation of the cosmic microwave background (CMB) radiation has provided state-of-the-art measurements on cosmological parameters. Measurements from the Wilkinson Microwave Anisotropy Probe (WMAP) and Planck satellite have pinned down the precision of the reionization optical depth τ to an unprecedented level, which essentially constrains the reionization process. There are two main effects of the reionization history on the CMB angular power spectra. The first effect is the photon attenuation effect; i.e., the ionized electron rescatters the CMB photons which leads to a suppression of the acoustic peaks in the CMB angular power spectra. So the amplitude of the C_ℓ^{TT} is proportional to $A_s e^{-2\tau}$, where A_s is the amplitude of the primordial curvature perturbations at the pivot scale $k_0 = 0.05 \text{ Mpc}^{-1}$. Given the same ionized hydrogen fraction, it contributes more to the optical depth if the reionization process began earlier and lasted longer. The second effect is the reionization bump in the C_ℓ^{TE} and C_ℓ^{EE} power spectra, as the polarization is generated due to the quadrupole seen by electrons after reionization. The angular position of the bump is proportional to the square root of the redshift at which the reionization occurs, while the amplitudes of C_ℓ^{TE} and C_ℓ^{EE} are proportional to τ and τ^2 respectively [1, 2]. Therefore, measurements of the large-scale polarization angular power spectra can strongly constrain the reionization history [3, 4]. The 9-year results of WMAP give an estimate of optical depth

$\tau = 0.089 \pm 0.014$ [5]. In the Planck 2015 analysis based on the temperature power spectra and low- ℓ polarization, the optical depth is found to be $\tau = 0.078 \pm 0.019$ [6]. Using the Planck-high frequency instrument E-mode polarization and temperature data, the Planck lollipop likelihood gives $\tau = 0.058 \pm 0.012$ [7].

However, since the value of τ is an integration of free electron density, the detailed process of reionization is still a mystery although we have a fairly precise measurement of τ . A steplike instantaneous reionization model is proposed by Lewis [8] and used in the Planck 2013 and 2015 cosmological results. Some variants of such a phenomenological model were considered to constrain the reionization history [7, 9, 10]. A semianalytical reionization model is proposed based on the relevant physics governing these processes, such as the inhomogeneous intergalactic medium (IGM) density distribution, three different sources of ionizing photons, and radiative feedback [11].

All of the above models are built based on our current knowledge of the reionization. If the ansatz of the reionization model is not accurate, the evaluated values of cosmological parameters may be biased. Therefore, it is important and necessary to constrain it in a relatively model-independent way. Hu and Holder [4] proposed the principal component analysis (PCA) of the reionization history to quantify the information contained in the large-scale E-mode polarization. This approach has been applied to both the simulated and real CMB data [12, 13]. In our previous work, we applied such a PCA method for the reionization history to Planck 2015 data and found that the Universe is not completely reionized at redshift $z \gtrsim 8.5$ at 95% confidence level (C.L.) [14]. The PCA method has been used to investigate the impacts of the reionization model on the estimates of cosmological parameters [15–20]. The estimated values of cosmological parameters such as the amplitude of the power spectrum

*Electronic address: daiwming@itp.ac.cn

†Electronic address: Ma@ukzn.ac.za

‡Electronic address: guozk@itp.ac.cn

§Electronic address: cairg@itp.ac.cn

of primordial scalar perturbations and neutrino masses are sensitive to the reionization history.

In addition, the evolution of the intergalactic Lyman-alpha ($\text{Ly}\alpha$) opacity measured in the spectra of quasars can provide valuable information on the reionization history [21]. The recent measurements imply that the reionization of the IGM was nearly completed at redshift $z \approx 6$ [22]. The detection of complete Gunn-Peterson (GP) absorption troughs in the spectra of quasars at $z > 6$ suggests that the neutral fraction of the IGM increases rapidly with redshift [23–27]. The rapid decline in the space density of $\text{Ly}\alpha$ emitting galaxies in the region $z = 6 - 8$ implies a low-redshift reionization process [28]. But probing the high-redshift reionization history directly is still a big challenge.

In this paper, we apply two different methods to constrain the reionization history: the widely used tanh parametrization method proposed by Lewis [8] and the PCA approach proposed by Hu and Holder [4]. Using the Planck 2015 data combined with spectroscopic observations, we investigate the constraints on the reionization history and cosmological parameters.

This paper is organized as follows. In Sec. 2, we describe the tanh parametrization and PCA methods respectively. In Sec. 3, we list the current measurements of the neutral hydrogen fraction. In Sec. 4, we use the Planck 2015 data and the neutral hydrogen fraction data to put constraints on the reionization history. Section 5 is devoted to discussions and conclusions.

2. METHODS

Throughout our analysis, we adopt a spatially flat Λ CDM model described by a set of cosmological parameters $\{\Omega_b h^2, \Omega_c h^2, \theta_{\text{MC}}, A_s, n_s\}$, where $\Omega_b h^2$ and $\Omega_c h^2$ are the physical baryon and cold dark matter densities relative to the critical density, θ_{MC} is an approximation to the ratio of the sound horizon to the angular diameter distance at the photon decoupling, A_s is the amplitude defined as in Sec. 1, and n_s is the spectral index of the primordial curvature perturbations at the pivot scale $k_0 = 0.05 \text{ Mpc}^{-1}$.

2.1. “tanh” function parametrization

The most widely used parametrization is a step like transition of the ionized hydrogen fraction x_e , which is parametrized by the median redshift z_{re} and duration Δz of the reionization. A tanh function is utilized to fit the reionization history [8]:

$$x_e^{\text{eff}}(z) = f * x_e(z) = \frac{f}{2} \left[1 + \tanh \left(\frac{y(z_{\text{re}}) - y}{\Delta y} \right) \right], \quad (1)$$

where $y = (1+z)^{3/2}$ and $\Delta y = 3/2(1+z)^{1/2}\Delta z$. Since the first ionization energy (24.6 MeV) of helium is not much

higher than hydrogen (13.6 MeV), it is usually assumed that helium first reionizes in the same way as hydrogen. Ignoring the residual electron density from recombination, the efficient reionization fraction is $x_e^{\text{eff}} \equiv f * x_e$. The factor x_e is the ratio between number densities of ionized hydrogen to the total hydrogen, and $f * x_e$ is the number density ratio between free electrons and total hydrogen. Therefore the factor f is $f = 1 + n_{\text{He}}/n_{\text{H}}$, where n_{He} and n_{H} are the number densities of helium and hydrogen respectively. The typical value of f is roughly 1.08 because the helium mass fraction is around 0.24. Additionally, we assume that hydrogen is fully ionized before the second helium ionization (the corresponding ionization energy is 54.4 MeV). Meanwhile, the helium second reionizes at $z_{\text{re}} = 3.5$ with the tanh parameters $f = n_{\text{He}}/n_{\text{H}}$ and $\Delta z = 0.5$. The total efficient reionization fraction is the sum of contributions from hydrogen and helium.

It is argued that the hydrogen in the IGM could have been reionized twice [29, 30], although spectroscopic observations have given a hint that the IGM ionization is similar to a phase transition and the follow-up study revealed that double reionization requires extreme parameter choices [31]. The simple parametrization described by Eq. (1) may bias the reionization history. To eliminate the bias, we can define discrete ionization fractions in a series of small redshift bins, which correlate with each other in practice.

2.2. Principal component analysis

The PCA method converts a set of correlated variables into a set of linear uncorrelated variables by an orthogonal transformation. Most information is encoded in the principal components, which are picked out according to their corresponding eigenvalues. Following Refs. [14, 32], we consider a binned ionization fraction $x_e(z_i)$, $i \in \{1, 2, \dots, N_z\}$, with redshift bins of width $\delta z = 0.25$. We take $z_{\text{min}} = 6$ and $z_{\text{max}} = 30$ with the definition $z_1 = z_{\text{min}} + \delta z$ and $z_{N_z} = z_{\text{max}} - \delta z$ so that $N_z + 1 = (z_{\text{max}} - z_{\text{min}})/\delta z$. The principal components of $x_e(z_i)$ are the eigenfunctions of the following Fisher matrix F_{ij} ,

$$F_{ij} = \sum_{\ell=2}^{\ell_{\text{max}}} \left(\ell + \frac{1}{2} \right) \frac{\partial \ln C_{\ell}^{\text{EE}}}{\partial x_e(z_i)} \frac{\partial \ln C_{\ell}^{\text{EE}}}{\partial x_e(z_j)}, \quad (2)$$

which describes the dependence of the polarization spectrum C_{ℓ}^{EE} on the ionization fraction $x_e(z_i)$. The Fisher matrix F_{ij} can be decomposed as

$$F_{ij} = (N_z + 1)^{-2} \sum_{\mu=1}^{N_z} S_{\mu}(z_i) \sigma_{\mu}^{-2} S_{\mu}(z_j), \quad (3)$$

where σ_{μ}^2 are the inverse eigenvalues and $S_{\mu}(z)$ are the eigenfunctions that satisfy the orthogonality and com-

pleteness relations

$$\int_{z_{\min}}^{z_{\max}} dz S_{\mu}(z) S_{\nu}(z) = (z_{\max} - z_{\min}) \delta_{\mu\nu}, \quad (4)$$

$$\sum_{\mu=1}^{N_z} S_{\mu}(z_i) S_{\mu}(z_j) = (N_z + 1) \delta_{ij}. \quad (5)$$

Then, the reionization history is represented in terms of the eigenfunctions as

$$x_e(z) = x_e^{\text{fid}}(z) + \sum_{\mu} m_{\mu} S_{\mu}(z). \quad (6)$$

The x_e^{fid} is the fiducial value of the hydrogen reionization fraction, we set $x_e^{\text{fid}} = 0.1$ in our fiducial models, and m_{μ} are the amplitudes of principal components. Mortonson and Hu [32] argued that $x_e(z)$ is not necessarily bounded in between 0 and 1 at all redshifts and derived a necessary but not sufficient condition for physicality. Nevertheless, in this paper, we simply assume that the selected principal components reconstruct the reionization history sufficiently well so that the bound is $x_e(z) \in [0, 1]$. The reason is that we combine the neutral hydrogen fraction data listed in Sec. 3 with CMB to fit the cosmological parameters and our reionization model has no impact on the neutral hydrogen fraction data (physically, $x_{\text{HI}} \in [0, 1]$, defined in Sec. 3).

Since the reionization history is reconstructed with only the first few eigenvectors, there are some residual errors to be corrected by the rest of the eigenvectors. In practice, we can regard these truncation errors as systematic errors introduced by the PCA method and make a rough estimate. We emphasize that any truncation of principal component decomposition provides the least squares approximation of the real reionization history as the eigenfunctions satisfy the orthogonality and completeness relations. Heinrich *et al.* quantitatively demonstrated that the first five eigenvectors form a complete representation of the observable impact on C_{ℓ}^{EE} of any given reionization history, but the representation is not complete in the ionization history itself [20]. The present data are incapable of putting a strict limit on the reionization history without any physical hypothesis, which means the possible function space $[z \mapsto x_e(z)]$ remains undetermined under this circumstance. Moreover, the principal component decomposition is carried out based on the cosmic variance limited C_{ℓ}^{EE} power spectrum instead of the real observation, which could loosen the constraint on the reionization history. In what follows, we illustrate the character of PCA reconstructed reionization history and estimate the systematic errors via two types of general reionization models.

To get rid of the unphysical curves, we generate the samples under the additional condition $0.03 < \tau < 0.13$, which is around 3σ width of Planck constraints. Figure 1 illustrates the cases of randomly sampled reionization history. Each curve connects the end points and

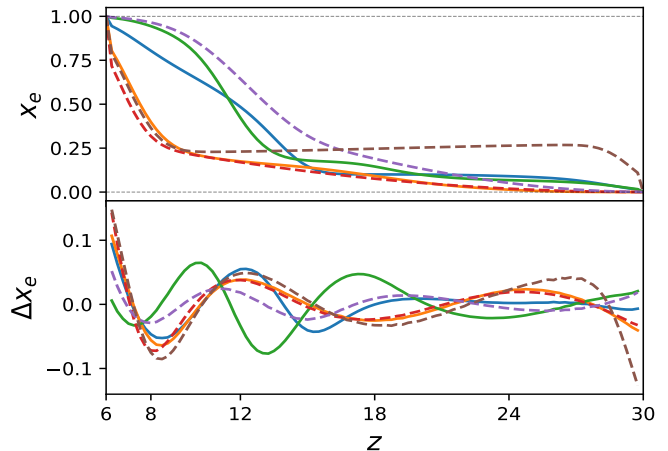


FIG. 1: Randomly sampled reionization history (upper panel) and the corresponding systematic errors of principal component decomposition (lower panel). Functions of $x_e(z)$ are constructed by connecting the randomly sampled knots and the end points with PCHIP. The solid lines are type (a) curves, while the dashed lines are type (b) curves. All of them are smoothed by Gaussian function with $\sigma = 4\delta z = 1.0$. Curves of $\Delta x_e(z)$ are clustered around $\Delta x_e(z) = 0$.

randomly sampled knots, while the interpolation function is a piecewise cubic Hermite interpolating polynomial (PCHIP). This approach makes sure that $x_e(z)$ is bounded in between 0 and 1. We consider two types of curves: (a) monotonically decreasing curves interpolated between the end points ($z = 6.0$ and $z = 30.0$) and five randomly sampled knots with PCHIP and (b) non-monotonic curves interpolated between the end points and two randomly sampled knots with PCHIP. All curves are smoothed by a Gaussian function. Then, we project $x_e(z)$ onto the eigenvectors and get the coefficients

$$m_{\mu} = \frac{\sum_i [x_e(z_i) - x_e^{\text{fid}}(z_i)] S_{\mu}(z_i)}{\sum_i S_{\mu}(z_i) S_{\mu}(z_i)}. \quad (7)$$

With Eq. (6), the PCA reconstruction is easy and straightforward. $\Delta x_e(z)$ is defined as the difference between PCA reconstructed and the true form of $x_e(z)$, which is sensitive to the reionization history.

Figure 2 shows the distribution of $\Delta x_e(z)$ within the redshift range $6.25 \leq z \leq 29.75$, assuming that each possible reionization history is of equal probability as in Fig. 1. It suggests that the PCA method is also likely to bias the reionization history, although it is independent of any physical hypothesis. But statistically, the bias is expected to be small for a general reionization curve. To estimate the possible systematic errors, we compute the probability density of $|\Delta x_e|_{\max}$, the maximal value of systematic errors of each reionization instance, as well as the probability density of $|\Delta x_e|_{\text{avg}}$, the average of systematic errors of each reionization instance, defined as $|\Delta x_e|_{\text{avg}} = \int_{z_{\min}}^{z_{\max}} |\Delta x_e(z)| dz / (z_{\max} - z_{\min})$.

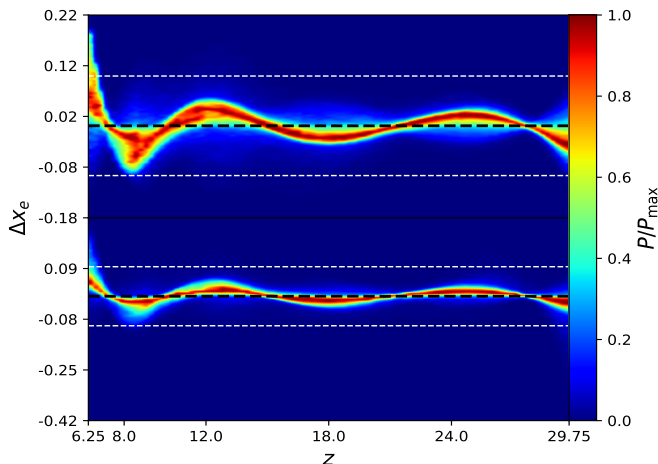


FIG. 2: Distribution of the systematic errors of the PCA method. The upper panel illustrates the type (a) curves, while the lower panel illustrates the type (b) curves. The black and white dashed horizontal lines show a band with width $\Delta x_e(z) \leq 0.1$, centered at $\Delta x_e(z) = 0$.

Figure 3 shows the probability density of the maximal errors $|\Delta x_e|_{\max}$ and the average errors $|\Delta x_e|_{\text{avg}}$. $|\Delta x_e|_{\text{avg}}$ is approximately bounded between 0 and 0.05 for all cases. In the case that the Gaussian smoothing scale is $\sigma = 1.0$, the boundary of the maximal error is $|\Delta x_e|_{\max} \lesssim 0.2$. The distribution can be sharpened by increasing the smoothing scale. That means the PCA method keeps the overall feature, but is incapable of catching the local property. The PCA method is applicable, since we investigate the reionization history in a large redshift range and probably lose the local details.

In what follows, “instant” denotes the parametrization method for the reionization history [Eq.(1)] and “PCA” denotes the PCA method (Eq.(6)). The former is described by the median redshift z_{re} and reionization duration Δz , while the latter is described by five parameters m_μ , $\mu = 1, \dots, 5$. In our analysis we use the publicly available CosmoMC package to explore the parameter space by means of the Markov chain Monte Carlo (MCMC) technique [33]. We modify the Boltzmann CAMB code [34] to appropriately incorporate the reionization history. The reionization parameters and other cosmological parameters are evaluated by performing global fitting in Sec. 4.

3. DATA

We list current constraints on the volume-averaged neutral hydrogen fraction in Table I. Table I summarizes the constraints on the neutral hydrogen fraction or free electron fraction over the redshift range $z = 5-8$ which were derived from 2006 to 2017. These constraints can be summarized into four categories.

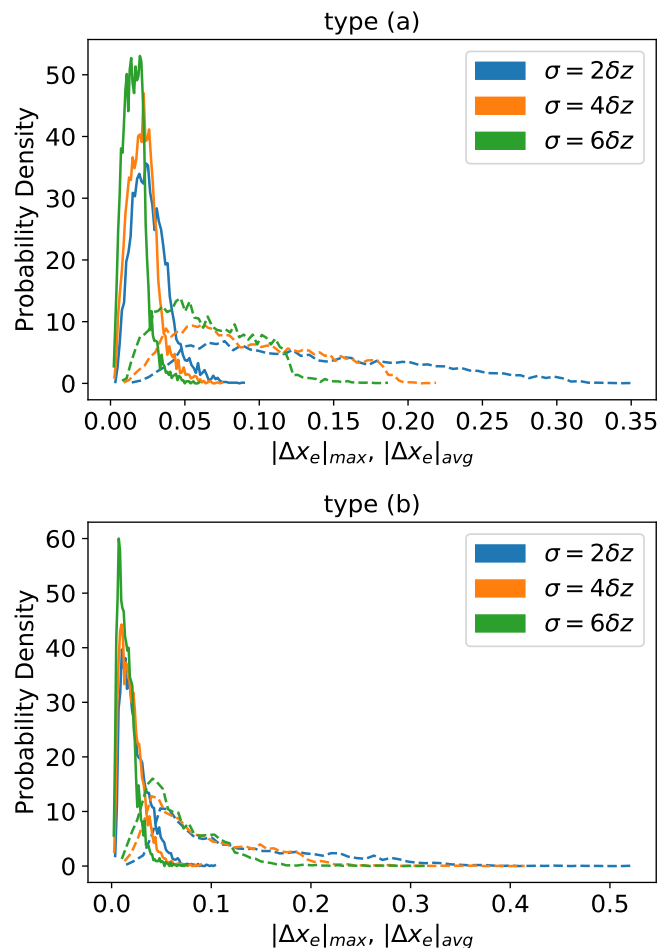


FIG. 3: Estimation on the systematic errors of the PCA method. The solid curves show the probability density of the average of $|\Delta x_e|$, while the dashed curves show the probability density of the maximal value of each reionization instance. Three smoothing scales of the reionization curves are plotted: $\sigma = 2\delta z = 0.5$, $\sigma = 4\delta z = 1.0$ and $\sigma = 6\delta z = 1.5$.

- Quasar/GRB Ly α absorption line systems [22, 36–40, 54].
 1. Fan *et al.* [22] used the GP optical depth and HII region size measurements around luminous quasars to measure that the reionization process finishes between $z = 5.9$ and $z = 6.5$.
 2. Gallerani *et al.* [36] and McGreer *et al.* [37] used quasar-stellar object (QSO) dark gap statistics and measured the fraction of neutral hydrogen to be very low at redshift $z \sim 5.6$.
 3. Schroeder *et al.* [38] used the GP damping wing of the spectra of three quasars (SDSS J1148+5251 ($z = 6.4189$), J1030+0524 ($z = 6.308$) and J1623+3112 ($z = 6.247$)), to constrain the neutral hydrogen fraction, $x_{\text{HI}} = 1 - x_e$, and found the lower limit of x_{HI} at

TABLE I: The current constraints on the neutral hydrogen fraction x_{HI} from different observations, ranging from low to high redshifts. “LAEs” means Ly α emitters, i.e. Ly α emitting galaxies.

Redshift z	x_{HI} data	C.L.	Technique	Observation	Ref.	Year	Dataset
5.03	$x_{\text{HI}} = (5.5 \times 10^{-5})_{-1.65 \times 10^{-5}}^{+1.42 \times 10^{-5}}$	1σ	GP optical depth of QSOs	SDSS	[22]	2006	Full
5.25	$x_{\text{HI}} = (6.7 \times 10^{-5})_{-2.44 \times 10^{-5}}^{+2.07 \times 10^{-5}}$	1σ			[35]		
5.45	$x_{\text{HI}} = (6.6 \times 10^{-5})_{-3.01 \times 10^{-5}}^{+2.47 \times 10^{-5}}$	1σ					
5.65	$x_{\text{HI}} = (8.8 \times 10^{-5})_{-4.60 \times 10^{-5}}^{+3.65 \times 10^{-5}}$	1σ					
5.85	$x_{\text{HI}} = (1.3 \times 10^{-4})_{-4.90 \times 10^{-5}}^{+4.08 \times 10^{-5}}$	1σ					
6.10	$x_{\text{HI}} = (4.3 \times 10^{-4}) \pm (3.0 \times 10^{-4})$	1σ					
5.3	$\log_{10} x_{\text{HI}} = -4.4_{-0.90}^{+0.84}$	1σ	QSO dark gap statistics	SDSS	[36]	2008	Full
5.6	$\log_{10} x_{\text{HI}} = -4.2_{-1.0}^{+0.84}$	1σ					
5.6	$x_{\text{HI}} < 0.04 + 0.05$	1σ	Counts of dark Lyman-alpha pixels	Keck II telescopes	[37]	2015	Full
5.9	$x_{\text{HI}} < 0.06 + 0.05$	1σ					
6.247	$x_{\text{HI}} \gtrsim 0.14$	2σ	QSO damping wing J1623+3112	SDSS	[38]	2013	Full/ext
6.308	$x_{\text{HI}} \gtrsim 0.11$	2σ			J1030+0524		
6.4189	$x_{\text{HI}} \gtrsim 0.14$	2σ			J1148+5251		
6.3	$x_{\text{HI}} = 0.0 \pm 0.17 \pm 0.60$	$1\sigma, 2\sigma$	Ly α damping wing of GRB 050904	Subaru Telescope	[39]	2006	Full/ext
6.3	$x_{\text{HI}} = (6.4 \pm 0.3) \times 10^{-5}$	1σ	GRB 050914 spectra	Swift satellite	[40]	2008	Not applicable
6.5	$x_{\text{HI}} \lesssim 0.3$	N/A	LAEs	Large-Area Lyman Alpha survey	[41]	2004	Not applicable
6.5	$0 \lesssim x_{\text{HI}} \lesssim 0.45$	N/A	17 LAEs	Subaru Deep Field and Keck	[42]	2006	Not applicable
6.6	$x_{\text{HI}} = 0.3 \pm 0.2$	1σ	2,354 LAEs	Subaru/Hyper Suprime-Cam survey	[43]	2017	Full/ext
6.6	$x_{\text{HI}} \lesssim 0.2 \pm 0.2$	N/A	207LAEs	subaru/XMM-Newton Deep Survey field	[44]	2010	Not applicable
6.6	$x_{\text{HI}} < 0.5$	2σ	Clustering of 58 LAEs	Subaru Deep Field	[45]	2007	Full/ext
6.6	$x_{\text{HI}} \simeq 0.24 - 0.36$	N/A	Model and observed Ly α luminosity function	Subaru Deep Field	[46]	2008	Not applicable
7.0	$x_{\text{HI}} \simeq 0.24 - 0.36$	N/A					
6.9	$x_{\text{HI}} = 0.4 - 0.6$	N/A	LAEs	DECam/Blanco telescope	[47]	2017	Not applicable
7.0	$x_{\text{HI}} = 0.39_{-0.09}^{+0.08}$	1σ	LAEs	Keck MOSFIRE spectrograph	[48]	2014	Full/ext
8.0	$x_{\text{HI}} > 0.64$	1σ					
7.0	$x_{\text{HI}} > 0.4^{\text{a}}$	1σ	Ly α fraction evolution	Numerical Simulation	[49]	2015	Full/ext
7.0	$x_{\text{HI}} \sim 0.5$	N/A	Prevalence of Ly α Emission in Galaxies	Vary Large Telescope	[50]	2014	Not applicable
7.0	$x_{\text{HI}} \sim 0.6 - 0.9$	N/A	Prevalence of Ly α Emission in Galaxies	Keck Telescope	[51]	2012	Not applicable
7.0	$x_{\text{HI}} \geq 0.51$	N/A	Prevalence of Ly α Emission in Galaxies	Vary Large Telescope	[52]	2014	Not applicable
7.0	$x_{\text{HI}} \lesssim 0.5$	1σ	Clustering of LAEs	Subaru Hyper Suprime-Cam	[53]	2015	Full/ext
7.085	$x_{\text{HI}} \gtrsim 0.1$	N/A	Quasar ULAS J1120 + 0641	UKIRT Infrared Deep Sky Survey	[54]	2011	Not applicable
7.085	$x_{\text{HI}} = 0.40_{-0.19-0.32}^{+0.21+0.41}$	$1\sigma, 2\sigma$	ULAS J1120 + 0641 damping wing	Magellan/Baade telescope	[55]	2017	Full/ext
8.0	$x_{\text{HI}} \gtrsim 0.3$	N/A	Prevalence of Ly α Emission in Galaxies	Keck Telescope	[56]	2014	Not applicable

^a Converted from ionized fraction. These data are derived from numerical simulation rather than observation.

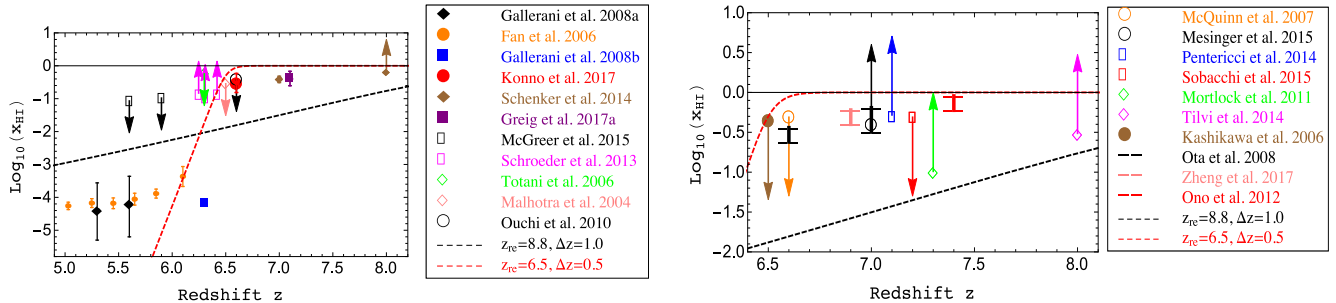


FIG. 4: The state-of-the-art measurement on $x_{\text{HI}}(z)$, taken from Table I. The black and red dashed lines are two examples of the “tanh” model which cannot fit the data very well.

$z \sim 6.2\text{--}6.4$.

4. Totani *et al.* [39] used the Ly α damping wing of GRB 050914 ($z = 6.3$) spectra to obtain the column density of HI, and derived the upper limit of x_{HI} to be $x_{\text{HI}} < 0.17$ and 0.60 at 68% and 95% C.L. respectively.
 5. Gallerani *et al.* [40] used the dark portions (gaps) in GRB 050904 absorption spectra to derive the neutral hydrogen fraction $x_{\text{HI}} = (6.4 \pm 0.3) \times 10^{-5}$ at $z = 6.29$.
 6. Mortlock *et al.* [54] reported a quasar (ULAS J112001.48+064124.3) at $z = 7.085$, and used the Ly α damping wing profile to obtain that the neutral fraction of the intergalactic medium in front of ULAS J1120+0641 exceeded 0.1. Using the same quasar, Greig *et al.* [55] accounted for uncertainties of the intrinsic QSO emission spectrum and the distribution of cosmic HI patches during the epoch of reionization (EoR) from simulation and reported that the EoR is not yet complete by $z = 7.1$, with the volume-weighted IGM neutral fraction constrained to be $x_{\text{HI}} = 0.40^{+0.21+0.41}_{-0.19-0.32}$ at 1σ and 2σ C.L.
- The number density and clustering of Ly α emitting galaxies [41–44, 46–48]. This type of observation is to use Ly α emitting galaxies to measure the Ly α luminosity functions and then by comparing the Ly α luminosity function measurements with reionization models, one can derive the neutral hydrogen fraction of the intergalactic medium x_{HI} . Such studies give the measurement of x_{HI} in the redshift range of 6.5 to 8.0.
 - Gravitational clustering of Ly α emitters [45, 53]. As shown in [45, 53], reionization increases the measured clustering of emitters, which can be computed observationally. By comparing the observational clustering of emitters with the results using radiative transfer simulations, McQuinn *et al.* [45] and Sobacchi and Mesinger. [53] obtained the upper limit of $x_{\text{HI}} \lesssim 0.5$ at $z = 6.6$ and 7.0 respectively.

- Prevalence of Ly α emission in galaxies at redshift 6–8 [50–52, 56]. This class of observation is to assume that Ly α emission is prevalent in star-forming galaxies at $z \sim 6.5\text{--}8$, which is a simple extrapolation of the observed prevalence at $z \sim 4\text{--}6$. Then any departure from these trends is due to an increasingly neutral IGM at $z \sim 7\text{--}8$. Therefore one can use this technique to quantify the filling factor of ionized hydrogen (Q_{HI}) at $z \sim 6.5\text{--}8$. Then one can convert this factor to IGM fractional neutral hydrogen density x_{HI} .

As marked in the last column of Table I, we divide the x_{HI} data into different datasets. Only the data with C.L. are used in our analysis, while the others are plotted in figures for comparison. The error bar is conservatively estimated if it is not given explicitly. For example, since a lower limit is given in Ref. [49] we assume that the mean value is $x_{\text{HI}} = 1$, and the mean value is $x_{\text{HI}} = 0$ for the upper limit given in Ref. [53]. Because the limit derived in Ref. [40] is much tighter than the others, we do not use these data in our analysis. In the PCA model, we assume that the reionized fraction x_e is exact unity at $z \leq 6.0$. The dataset of x_{HI} used to constrain the reionization history in the PCA model is denoted by “ext” in Table I. All data given with confidence level can be used in the instant model, which is denoted by “full.” Based on the common instant reionization assumption, we obtain a tanh model of x_{HI} increasing with z . The tanh model is intuitively compared with x_{HI} data in Fig. 4 with ($z_{\text{re}} = 8.8, \Delta z = 1.0$) and ($z_{\text{re}} = 6.5, \Delta z = 0.5$). For these two selective values, the tanh model cannot match the data very well.

4. RESULTS

In our analysis, besides the neutral hydrogen fraction data, we use Planck 2015 likelihood code and data, including the Planck low- ℓ likelihood at multipoles $2 \leq \ell \leq 29$ and high- ℓ PlikTT likelihood at multipoles $\ell \geq 30$ based on pseudo- C_ℓ estimators. The low- ℓ likelihood uses the foreground-cleaned LFI 70 GHz polarization

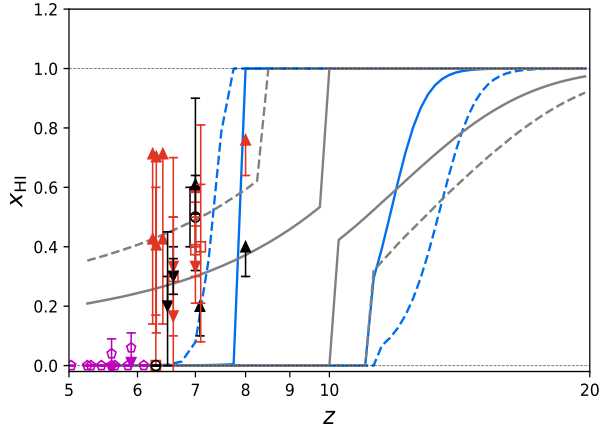


FIG. 5: Limits on x_{HI} at redshift ranging from 5 to 20 in the instant reionization model, with 68% (solid) and 95% (dashed) confidence regions, derived from Planck 2015 + full data (blue) and Planck 2015 (gray) respectively. The red and magenta points as well as error bars belong to the full dataset as marked in Table I, while the black points and error bars are not applicable in our analysis and just plotted for visual comparison

maps together with the temperature map obtained from the Planck 30 to 353 GHz channels by the Commander component separation algorithm over 94% of the sky. The high- ℓ PlikTT likelihood uses 100, 143, and 217 GHz cross-half-mission temperature spectra, avoiding the Galactic plane as well as the brightest point sources and the regions where the CO emission is the strongest. Hereafter, “Planck 2015” denotes the combination of the PlikTT temperature likelihood and the low- ℓ temperature-polarization likelihood.

We constrain the instant model of the EoR with Planck 2015 data and the full x_{HI} data. We reconstruct the EoR during the redshift interval $5 < z < 20$ in Fig. 5. The transition occurs at the redshift ranging from $z \sim 8$ to 14. The reconstructed figure is not fully consistent with the x_{HI} data. Meanwhile, in Fig. 6, we see that the posterior distributions of τ , z_{re} and Δz are bimodal. This means the instant model may bias the EoR. The 2D contours derived from Planck 2015 + ext are also plotted in Fig. 6. There are no x_{HI} data at redshift $z < 6$ in the ext dataset, which means we remove the limit that the Universe is fully ionized at $z \sim 6$ in this model. But the estimated median redshift and duration of reionization are $z_{\text{re}} \sim 8$ and $\Delta z \gtrsim 8$. This gives an unphysical result that the Universe is still not fully ionized today.

We constrain the PCA model of EoR with Planck 2015 + ext data, with a redshift interval of $6 < z < 30$. As plotted in Fig. 7, the reconstructed $x_{\text{HI}}(z)$ function covers the x_{HI} data. The error bar of the optical depth τ is smaller than in the instant model as shown in Table II. Comparing the confidence regions derived from Planck

2015 + ext data (blue) and Planck 2015 (gray) in Fig. 7, we see that constraints on x_e between $z \sim 6$ and $z \sim 10$ are strengthened with the help of x_{HI} data. But the additional data do not have a significant impact on the high-redshift EoR.

We also limit the range of reconstruction to be $6 < z < 20$ in the PCA model, and we obtain that the mean value of τ decreases by about 1σ C.L. The reconstructed EoR is shown in Fig. 8. The confidence regions are stretched with the increase of z_{end} , because τ is an integral $\int x_e^{\text{eff}} n_{\text{H}} dt$ and the Planck data are more sensitive to τ than the detailed reionization process [7].

Table II summarizes the constraints on the EoR and other cosmological parameters from the Planck 2015 and x_{HI} data. Bounds on parameters are nearly unchanged between different models, except the parameters of detailed reionization, the optical depth τ , the degenerated parameter A_s and the rms matter fluctuations today in linear theory σ_8 . The amplitude of the primordial spectrum of scalar perturbations A_s degenerates with optical depth τ in the form $A_s e^{-2\tau}$ on the small scale [57], which means that a large τ leads to a large A_s and σ_8 . In the PCA model with a redshift interval of $6 < z < 30$, the marginalized 2D contours (68% and 95% C.L.) and posterior distributions for m_μ derived from Planck 2015 + ext and Planck 2015 are shown in Fig. 9. The ext x_{HI} dataset is consistent with Planck 2015 data. Constraints on the amplitudes of principal components m_μ are significantly improved in the joint analysis of Planck 2015 and ext data.

5. DISCUSSION AND CONCLUSIONS

We have derived constraints on the cosmic reionization history using Planck temperature and low- ℓ polarization power spectra together with the neutral hydrogen fraction data in the Λ CDM model. We studied the commonly adopted tanh parametrization and the PCA reionization model. It gives unphysical results if we use the combined Planck 2015 data and the ext x_{HI} dataset to constrain the instant model. Meanwhile, our results show significant tension after adding the full x_{HI} dataset in the instant model. We may infer that the assumed instant model is oversimplified when the neutral hydrogen fraction data are included.

The PCA model is introduced to eliminate the model-dependent bias. In the PCA model, the reconstructed x_{HI} is consistent with x_{HI} data. Constraints on the low-redshift ($z \lesssim 10$) cosmic reionization history are significantly improved with the help of x_{HI} data; nevertheless, we find that the low-redshift x_{HI} data are nearly unhelpful for the high-redshift ($z \gtrsim 10$) constraints on x_{HI} when combined with Planck 2015 data. From the reconstructed reionization history, both in the case of redshift ranging from 6 to 30 and 6 to 20, we find that the Universe began to reionize at redshift no later than $z = 10$ at 95% C.L. Quantitatively, we derive the constraints on

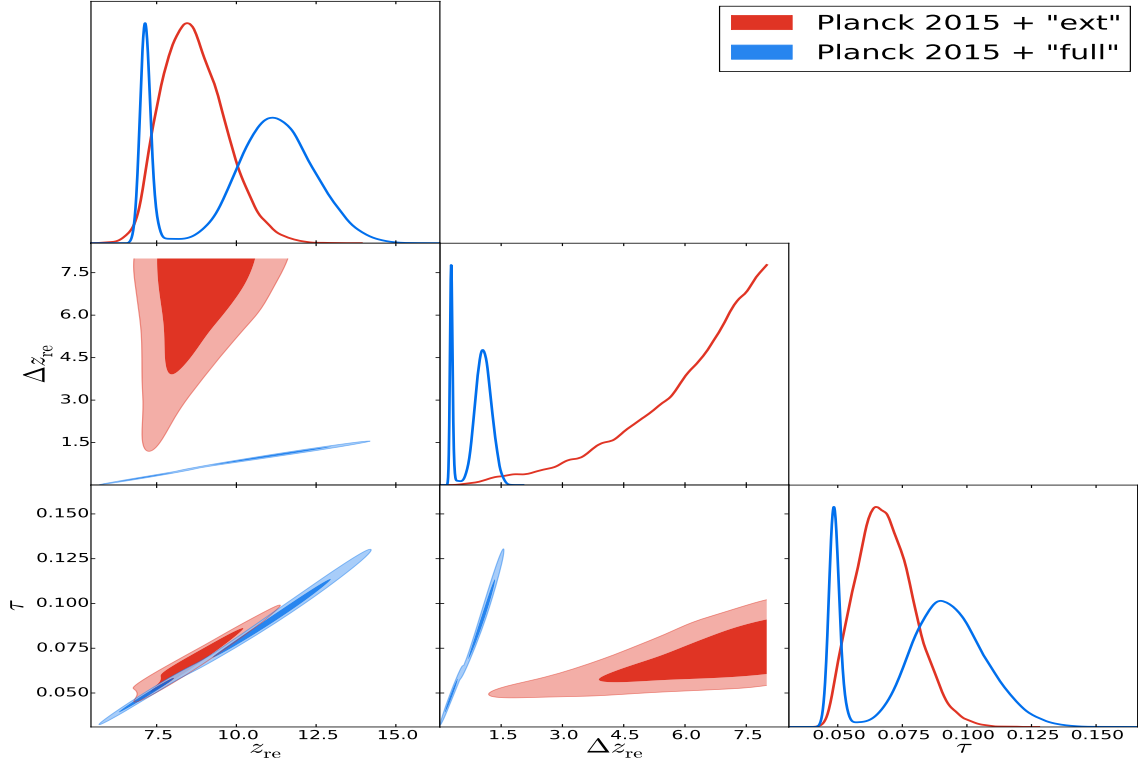


FIG. 6: Marginalized 2D contours (68% and 95% C.L.) and posterior distributions for parameters of the instant reionization model, derived from Planck 2015 + full (blue) and Planck 2015 + ext (red) respectively.

TABLE II: Mean values and marginalized 68% C.L. for reionization parameters and other cosmological parameters.

Model	Planck 2015 + ext		Planck 2015 + full
	PCA $6 < z < 30$	PCA $6 < z < 20$	Instant
$\Omega_b h^2$	0.02233 ± 0.00023	0.02227 ± 0.00022	0.02225 ± 0.00023
$\Omega_c h^2$	0.1187 ± 0.0021	0.1192 ± 0.0021	0.1195 ± 0.0022
$100\theta_{MC}$	1.04102 ± 0.00047	1.04095 ± 0.00046	1.04090 ± 0.00048
τ	0.110 ± 0.014	0.098 ± 0.013	$0.083^{+0.021+0.039}_{-0.038-0.040}$
n_s	0.9691 ± 0.0062	0.9674 ± 0.0060	0.9661 ± 0.0062
$\ln(10^{10} A_s)$	3.151 ± 0.026	3.128 ± 0.024	3.099 ± 0.044
H_0 (km s $^{-1}$ Mpc $^{-1}$)	67.82 ± 0.93	67.58 ± 0.94	67.43 ± 0.99
σ_8	0.852 ± 0.012	0.844 ± 0.011	0.833 ± 0.017
Age (Gyr)	13.792 ± 0.037	13.802 ± 0.037	13.807 ± 0.017
Ω_Λ	0.692 ± 0.013	0.689 ± 0.013	0.686 ± 0.014
Ω_m	0.308 ± 0.013	0.311 ± 0.013	0.314 ± 0.014
m_1	0.070 ± 0.039	0.204 ± 0.073	Not applicable
m_2	-0.070 ± 0.056	-0.124 ± 0.083	Not applicable
m_3	0.098 ± 0.053	0.120 ± 0.069	Not applicable
m_4	-0.052 ± 0.041	-0.040 ± 0.068	Not applicable
m_5	0.082 ± 0.042	0.031 ± 0.061	Not applicable
z_{re}	Not applicable	Not applicable	$10.29^{+1.97+3.30}_{-3.46-3.62}$
Δz	Not applicable	Not applicable	$0.87^{+0.37+0.49}_{-0.50-0.69}$

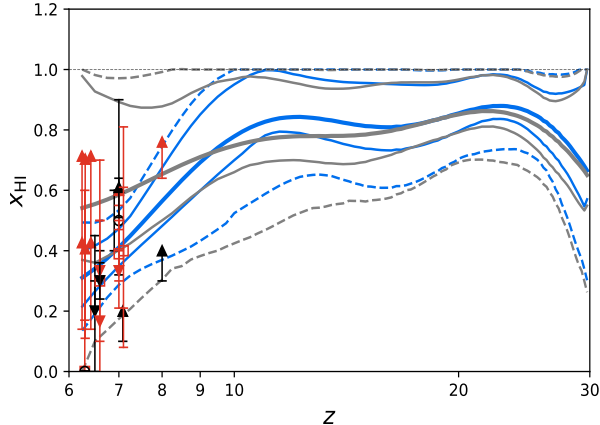


FIG. 7: Limits on x_{HI} at redshift ranging from 6 to 30 in the PCA model, with 68% (solid) and 95% (dashed) confidence regions and mean values (thick solid), derived from Planck 2015 + ext data (blue) and Planck 2015 (gray) respectively. The red points as well as error bars belong to the ext dataset as marked in Table I, while the black points and error bars are not applicable in our analysis and just plotted for visual comparison.

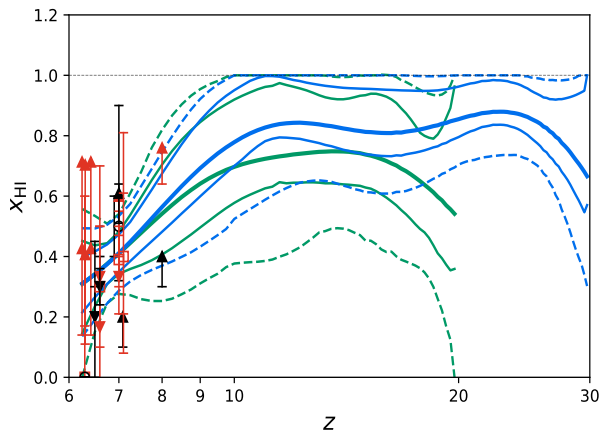


FIG. 8: Limits on x_{HI} at redshift ranging from 6 to 20 (green) and 6 to 30 (blue) in the PCA model, with 68% (solid) and 95% (dashed) confidence regions and mean values (thick solid), derived from Planck 2015 + ext data. The red points as well as error bars belong to the ext dataset as marked in Table I, while the black points and error bars are not applicable in our analysis and just plotted for visual comparison.

x_{HI} at $z = 9.75$ for both $6 < z < 20$ and $6 < z < 30$

redshift range reconstruction, and we find

$$x_{\text{HI}}(z = 9.75) = 0.69^{+0.30}_{-0.32}, \quad (8)$$

for $6 < z < 20$ reconstruction, and

$$x_{\text{HI}}(z = 9.75) = 0.76^{+0.22}_{-0.27}, \quad (9)$$

for $6 < z < 30$ reconstruction.

In the PCA model, the mean value of reionization optical depth is higher than but consistent with that obtained in the instant model. As is shown in Fig. 7, lacking direct measurements on the reionization at high redshift, constraints on the EoR are strengthened at low redshift $z \lesssim 10$ but remain nearly unchanged at high redshift $z \gtrsim 10$ by means of Planck 2015 and the x_{HI} data. The high-redshift EoR is only constrained by Planck 2015 data, which puts the upper limits on x_e (the lower limits on x_{HI}). The uncertainty of x_e in the high-redshift epoch leads to a higher optical depth. The current data are incapable of constraining the high-redshift ($z \gtrsim 10$) cosmic reionization history model independently. Recently, Bowman *et al.* [58] reported an absorption profile in the sky-averaged radio spectrum of the 21-cm signal detected with the Experiment to Detect the Global Epoch of Reionization Signature (EDGES) low-band instruments. Experiments using interferometric arrays (e.g. LOFAR [59], MWA [60], PAPER [61, 62], HERA [63] and SKA [64]) aimed at measuring the 21-cm signal from neutral hydrogen during the EoR have made progress. These future experiments will probe the reionization at high redshift directly and determine the reionization process eventually, which will also break the degeneracy between the reionization optical depth and other cosmological parameters such as the amplitude of the power spectrum of primordial scalar perturbations and neutrino masses [65].

Acknowledgments

Our numerical analysis was performed on the “Era” of Supercomputing Center, Computer Network Information Center of Chinese Academy of Sciences. Y.Z.M. is supported by the National Research Foundation of South Africa with Grant No.105925. Z.K.G. is supported by the National Natural Science Foundation of China Grants No. 11690021, No. 11575272 and No. 11335012. R.G.C. is supported by the National Natural Science Foundation of China Grants No. 11690022, No. 11435006 and No. 11647601; by the Strategic Priority Research Program of CAS Grant No. XDB23030100; and by the Key Research Program of Frontier Sciences of CAS.

[1] M. Zaldarriaga, Phys. Rev. **D55**, 1822 (1997), astro-ph/9608050.

[2] W. Hu and M. J. White, Astrophys. J. **479**, 568 (1997),

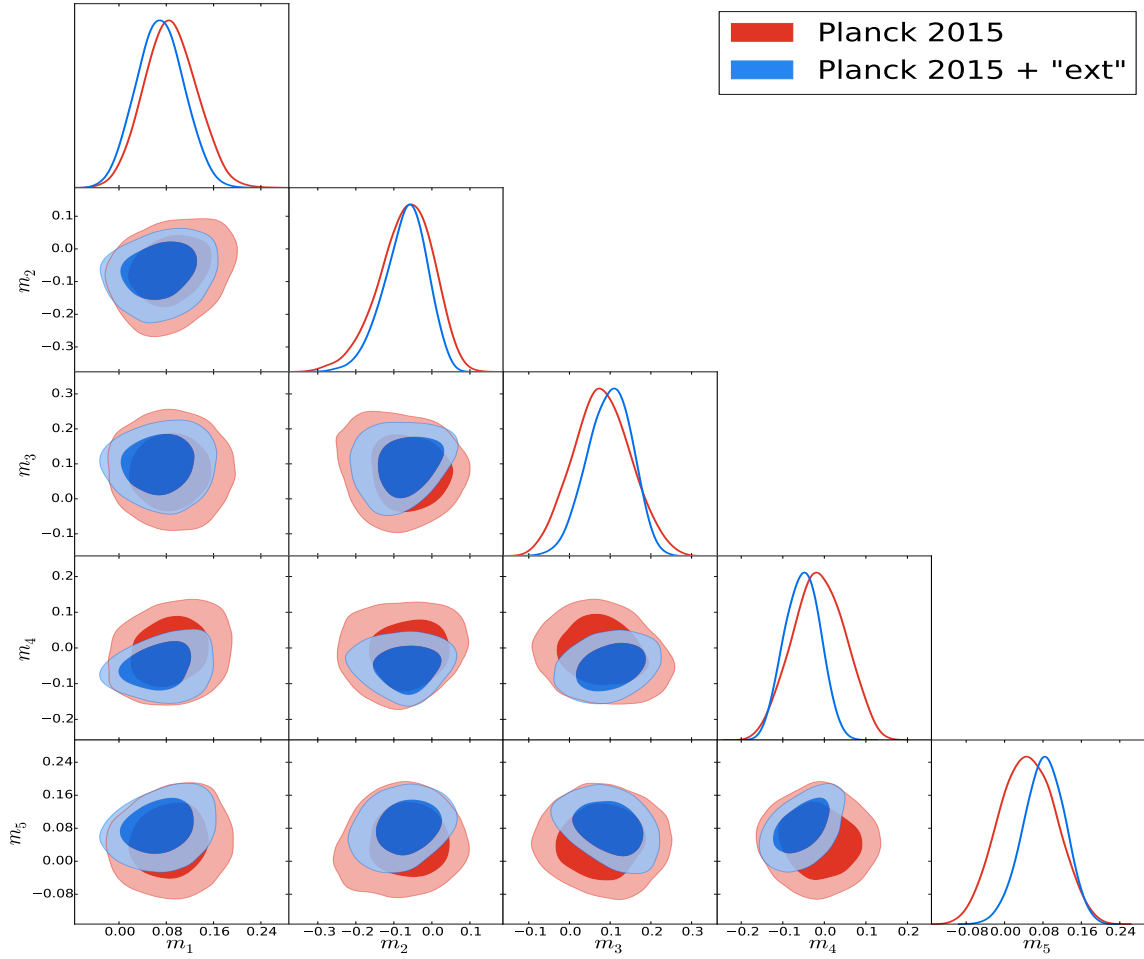


FIG. 9: Marginalized 2D contours (68% and 95% C.L.) and posterior distributions for m_μ , derived from Planck 2015 (red) and Planck 2015 + ext data (blue).

- astro-ph/9609079.
- [3] M. Kaplinghat, M. Chu, Z. Haiman, G. Holder, L. Knox, and C. Skordis, *Astrophys. J.* **583**, 24 (2003), astro-ph/0207591.
- [4] W. Hu and G. P. Holder, *Phys. Rev.* **D68**, 023001 (2003), astro-ph/0303400.
- [5] C. L. Bennett et al. (WMAP), *Astrophys. J. Suppl.* **208**, 20 (2013), 1212.5225.
- [6] P. A. R. Ade et al. (Planck), *Astron. Astrophys.* **594**, A13 (2016), 1502.01589.
- [7] R. Adam et al. (Planck), *Astron. Astrophys.* **596**, A108 (2016), 1605.03507.
- [8] A. Lewis, *Phys. Rev.* **D78**, 023002 (2008), 0804.3865.
- [9] M. Douspis, N. Aghanim, S. Ilić, and M. Langer, *Astrophys. J.* **580**, L4 (2015), 1509.02785.
- [10] A. L. Faisst, P. Capak, C. M. Carollo, C. Scarlata, and N. Scoville, *Astrophys. J.* **788**, 87 (2014), 1402.3604.
- [11] T. R. Choudhury and A. Ferrara, *Mon. Not. Roy. Astron. Soc.* **361**, 577 (2005), astro-ph/0411027.
- [12] L. P. L. Colombo and E. Pierpaoli, *New Astron.* **14**, 269 (2009), 0804.0278.
- [13] M. J. Mortonson and W. Hu, *Astrophys. J.* **686**, L53 (2008), 0804.2631.
- [14] W.-M. Dai, Z.-K. Guo, and R.-G. Cai, *Phys. Rev.* **D92**, 123521 (2015), 1509.01501.
- [15] M. J. Mortonson and W. Hu, *Phys. Rev.* **D77**, 043506 (2008), 0710.4162.
- [16] M. J. Mortonson, C. Dvorkin, H. V. Peiris, and W. Hu, *Phys. Rev.* **D79**, 103519 (2009), 0903.4920.
- [17] M. Archidiacono, A. Cooray, A. Melchiorri, and S. Pandolfi, *Phys. Rev.* **D82**, 087302 (2010), 1010.5757.
- [18] Y. Liu, H. Li, S.-Y. Li, Y.-P. Li, and X. Zhang, *JCAP* **1602**, 046 (2016), 1512.07394.
- [19] Q.-G. Huang and K. Wang, *JCAP* **1707**, 042 (2017), 1704.08495.
- [20] C. H. Heinrich, V. Miranda, and W. Hu, *Phys. Rev.* **D95**, 023513 (2017), 1609.04788.
- [21] J. E. Gunn and B. A. Peterson, *Astrophys. J.* **142**, 1633 (1965).
- [22] X.-H. Fan, M. A. Strauss, R. H. Becker, R. L. White, J. E. Gunn, G. R. Knapp, G. T. Richards, D. P. Schneider, J. Brinkmann, and M. Fukugita, *Astron. J.* **132**, 117 (2006), astro-ph/0512082.
- [23] R. Cen and P. McDonald, *Astrophys. J.* **570**, 457 (2002), astro-ph/0110306.
- [24] X. Fan, V. K. Narayanan, M. A. Strauss, R. L. White,

- R. H. Becker, L. Pentericci, and H.-W. Rix, *Astron. J.* **123**, 1247 (2002), astro-ph/0111184.
- [25] A. Lidz, L. Hui, M. Zaldarriaga, and R. Scoccimarro, *Astrophys. J.* **579**, 491 (2002), astro-ph/0111346.
- [26] R. L. White, R. H. Becker, X.-H. Fan, and M. A. Strauss, *Astron. J.* **126**, 1 (2003), astro-ph/0303476.
- [27] N. Y. Gnedin, *Astrophys. J.* **610**, 9 (2004), astro-ph/0403699.
- [28] T. R. Choudhury, E. Puchwein, M. G. Haehnelt, and J. S. Bolton, *Mon. Not. Roy. Astron. Soc.* **452**, 261 (2015), 1412.4790.
- [29] J. S. B. Wyithe and A. Loeb, *Astrophys. J.* **586**, 693 (2003), astro-ph/0209056.
- [30] R. Cen, *Astrophys. J.* **591**, 12 (2003), astro-ph/0210473.
- [31] S. Furlanetto and A. Loeb, *Astrophys. J.* **634**, 1 (2005), astro-ph/0409656.
- [32] M. J. Mortonson and W. Hu, *Astrophys. J.* **672**, 737 (2008), 0705.1132.
- [33] A. Lewis and S. Bridle, *Phys. Rev.* **D66**, 103511 (2002), astro-ph/0205436.
- [34] A. Lewis, A. Challinor, and A. Lasenby, *Astrophys. J.* **538**, 473 (2000), astro-ph/9911177.
- [35] R. J. Bouwens, G. D. Illingworth, P. A. Oesch, J. Caruana, B. Holwerda, R. Smit, and S. Wilkins, *Astrophys. J.* **811**, 140 (2015), 1503.08228.
- [36] S. Gallerani, A. Ferrara, X. Fan, and T. R. Choudhury, *Mon. Not. Roy. Astron. Soc.* **386**, 359 (2008), 0706.1053.
- [37] I. McGreer, A. Mesinger, and V. D'Odorico, *Mon. Not. Roy. Astron. Soc.* **447**, 499 (2015), 1411.5375.
- [38] J. Schroeder, A. Mesinger, and Z. Haiman, *Mon. Not. Roy. Astron. Soc.* **428**, 3058 (2013), 1204.2838.
- [39] T. Totani, N. Kawai, G. Kosugi, K. Aoki, T. Yamada, M. Iye, K. Ohta, and T. Hattori, *Publ. Astron. Soc. Jap.* **58**, 485 (2006), astro-ph/0512154.
- [40] S. Gallerani, R. Salvaterra, A. Ferrara, and T. R. Choudhury, *Mon. Not. Roy. Astron. Soc.* **388**, L84 (2008), 0710.1303.
- [41] S. Malhotra and J. E. Rhoads, *Astrophys. J.* **617**, L5 (2004), astro-ph/0407408.
- [42] N. Kashikawa et al., *Astrophys. J.* **648**, 7 (2006), astro-ph/0604149.
- [43] A. Konno, M. Ouchi, T. Shibuya, Y. Ono, K. Shimasaku, Y. Taniguchi, T. Nagao, M. A. R. Kobayashi, M. Kajisawa, N. Kashikawa, et al., *ArXiv e-prints* (2017), 1705.01222.
- [44] M. Ouchi et al., *Astrophys. J.* **723**, 869 (2010), 1007.2961.
- [45] M. McQuinn, L. Hernquist, M. Zaldarriaga, and S. Dutta, *Mon. Not. Roy. Astron. Soc.* **381**, 75 (2007), 0704.2239.
- [46] K. Ota et al., *Astrophys. J.* **677**, 12 (2008), 0707.1561.
- [47] Z.-Y. Zheng et al., *Astrophys. J.* **842**, L22 (2017), 1703.02985.
- [48] M. A. Schenker, R. S. Ellis, N. P. Konidaris, and D. P. Stark, *Astrophys. J.* **795**, 20 (2014), 1404.4632.
- [49] A. Mesinger, A. Aykutaalp, E. Vanzella, L. Pentericci, A. Ferrara, and M. Dijkstra, *Mon. Not. Roy. Astron. Soc.* **446**, 566 (2015), 1406.6373.
- [50] J. Caruana, A. J. Bunker, S. M. Wilkins, E. R. Stanway, S. Lorenzoni, M. J. Jarvis, and H. Ebert, *Mon. Not. Roy. Astron. Soc.* **443**, 2831 (2014), 1311.0057.
- [51] Y. Ono et al., *Astrophys. J.* **744**, 83 (2012), 1107.3159.
- [52] L. Pentericci et al., *Astrophys. J.* **793**, 113 (2014), 1403.5466.
- [53] E. Sobacchi and A. Mesinger, *Mon. Not. Roy. Astron. Soc.* **453**, 1843 (2015), 1505.02787.
- [54] D. J. Mortlock et al., *Nature* **474**, 616 (2011), 1106.6088.
- [55] B. Greig, A. Mesinger, Z. Haiman, and R. A. Simcoe, *Mon. Not. Roy. Astron. Soc.* **466**, 4239 (2017), 1606.00441.
- [56] V. Tilvi, C. Papovich, S. L. Finkelstein, J. Long, M. Song, M. Dickinson, H. Ferguson, A. M. Koekemoer, M. Gialaisco, and B. Mobasher, *Astrophys. J.* **794**, 5 (2014), 1405.4869.
- [57] P. A. R. Ade et al. (Planck), *Astron. Astrophys.* **571**, A16 (2014), 1303.5076.
- [58] J. D. Bowman, A. E. E. Rogers, R. A. Monsalve, T. J. Mozdzen, and N. Mahesh, *Nature* **555**, 67 (2018).
- [59] S. Zaroubi, A. G. de Bruyn, G. Harker, R. M. Thomas, P. Labropoulos, V. Jelić, L. V. E. Koopmans, M. A. Brentjens, G. Bernardi, B. Ciardi, et al., *Monthly Notices of the Royal Astronomical Society* **425**, 2964 (2012), 1205.3449.
- [60] J. S. Dillon, A. Liu, C. L. Williams, J. N. Hewitt, M. Tegmark, E. H. Morgan, A. M. Levine, M. F. Morales, S. J. Tingay, G. Bernardi, et al., *Physical Review D* **89**, 023002 (2014), 1304.4229.
- [61] Z. S. Ali, A. R. Parsons, H. Zheng, J. C. Pober, A. Liu, J. E. Aguirre, R. F. Bradley, G. Bernardi, C. L. Carilli, C. Cheng, et al., *The Astrophysical Journal* **809**, 61 (2015), 1502.06016.
- [62] J. C. Pober, Z. S. Ali, A. R. Parsons, M. McQuinn, J. E. Aguirre, G. Bernardi, R. F. Bradley, C. L. Carilli, C. Cheng, D. R. DeBoer, et al., *The Astrophysical Journal* **809**, 62 (2015), 1503.00045.
- [63] A. Liu and A. R. Parsons, *Monthly Notices of the Royal Astronomical Society* **457**, 1864 (2016), 1510.08815.
- [64] A. Mesinger, A. Ferrara, B. Greig, I. Iliev, G. Mellema, J. Pritchard, and M. Santos, *Advancing Astrophysics with the Square Kilometre Array (AASKA14)* 11 (2015), 1501.04106.
- [65] A. Liu, J. R. Pritchard, R. Allison, A. R. Parsons, U. Seljak, and B. D. Sherwin, *Phys. Rev.* **D93**, 043013 (2016), 1509.08463.